JGR Oceans

RESEARCH ARTICLE
10.1029/2025JC022457

Special Collection:
Years of the Maritime Continent

The Equatorial Deep Ocean Structure Associated With the Madden-Julian Oscillation From an Ocean Reanalysis

Connor Robbins[1], **Adrian J. Matthews**[1,2], **Rob A. Hall**[1], **Ben G. M. Webber**[1,3], and **Karen J. Heywood**[1]

[1]Centre for Ocean and Atmospheric Sciences, School of Environmental Sciences, University of East Anglia, Norwich, UK, [2]School of Engineering, Mathematics and Physics, University of East Anglia, Norwich, UK, [3]Climatic Research Unit, School of Environmental Sciences, University of East Anglia, Norwich, UK

Abstract

The Madden-Julian Oscillation (MJO) is the dominant weather system in the tropics on week-to-week time scales. Here, we exploit almost two decades of Argo float observations, assimilated into an ocean reanalysis, to examine the deep ocean response to the MJO. A coherent MJO signal in potential density and zonal velocity anomalies is observed down to at least 2,000 m (the typical maximum depth of Argo observations) in the Pacific and Indian Ocean basins, but not in the Atlantic. The signal is consistent with equatorial Kelvin wave structures. Below the thermocline, the anomalies are characterized by a vertical tilt, downward and to the east. Two theoretical frameworks are used to interpret the signal. The vertical mode framework is reasonably successful in representing the eastward propagation of equatorial Kelvin waves in the thermocline. The first internal mode is efficiently forced by the MJO surface winds, and energy is transferred to the second, third, and higher internal modes through nonlinear processes. However, these vertical modes are not useful for interpreting the deeper structure. Instead, ray paths are constructed using a vertically propagating wave framework. Rays forced by the low-frequency component of the MJO (with periods near 60 days) are consistent with the vertical tilt of the observed response. These ray paths explain the observed "shadow zones," where no coherent signal is found within 6,000 km of the western boundary of each ocean basin at 2,000 m depth.

Plain Language Summary

The Madden-Julian Oscillation (MJO) is a large weather system that lasts several weeks and changes rainfall, cloudiness, and winds over the tropics. The changes in wind speed and direction will potentially trigger a response in the deep tropical oceans. Argo floats began to routinely observe the deep ocean in the early 2000s; therefore, there are now two decades of data, enough to do a robust study of the MJO impact on the deep ocean. We observed an MJO signal in currents, temperature, and salinity in the equatorial Pacific and Indian Oceans down to at least 2,000 m (the maximum depth of Argo measurements). The signal is due to equatorial Kelvin waves (large-scale waves in the interior of the ocean) that propagate eastward and downward from the surface where they are forced by the MJO wind changes. As the tropical oceans are divided into three main basins, with continents in between, this eastward and downward propagation leads to the formation of shadow zones in the deep ocean at the western sides of the basin where no waves can reach. This is potentially important for mixing in the deep ocean, a poorly understood but crucial component of the global climate system.

Key Points:

- Deep ocean structure of Madden-Julian Oscillation from an ocean reanalysis in Pacific and Indian Oceans is an equatorial Kelvin wave
- Horizontal speed of the MJO signal in thermocline is consistent with the first internal mode structure with energy transfer to higher modes
- Kelvin wave downward and eastward ray paths lead to shadow zones in the deep ocean on the western boundary with no MJO signal

Supporting Information:

Supporting Information may be found in the online version of this article.

Correspondence to:

A. J. Matthews,
a.j.matthews@uea.ac.uk

Citation:

Robbins, C., Matthews, A. J., Hall, R. A., Webber, B. G. M., & Heywood, K. J. (2025). The equatorial deep ocean structure associated with the Madden-Julian Oscillation from an ocean reanalysis. *Journal of Geophysical Research: Oceans*, *130*, e2025JC022457. https://doi.org/10.1029/2025JC022457

Received 6 FEB 2025
Accepted 28 JUL 2025

Author Contributions:

Conceptualization: Connor Robbins, Adrian J. Matthews, Rob A. Hall, Ben G. M. Webber, Karen J. Heywood
Funding acquisition: Connor Robbins, Adrian J. Matthews
Methodology: Connor Robbins, Adrian J. Matthews, Rob A. Hall, Ben G. M. Webber, Karen J. Heywood
Project administration: Connor Robbins, Adrian J. Matthews
Software: Connor Robbins, Adrian J. Matthews

1. Introduction

The Madden-Julian Oscillation (MJO) is the dominant mode of intraseasonal variability in the tropical atmosphere (Jiang et al., 2020; Madden & Julian, 1972; Zhang, 2005; Zhang et al., 2020). It is primarily a long-lived tropical weather system, where a large (~10,000 km) region of enhanced convection and precipitation moves slowly eastward from the Indian Ocean, through the Maritime Continent (archipelago of Indonesia and neighboring countries) and into the western Pacific. The MJO precipitation anomalies are accompanied by wind, temperature, and pressure anomalies in the tropical atmosphere. Extreme rainfall is significantly more likely to be experienced within the active convective center of the MJO (Da Silva & Matthews, 2021). Additionally, the tropical MJO triggers an extratropical and global atmospheric circulation response, such that medium-range weather forecast skill depends in large part on the ability of a model to accurately simulate the MJO (Kent et al., 2022).

Supervision: Connor Robbins, Adrian J. Matthews, Rob A. Hall, Karen J. Heywood
Validation: Connor Robbins, Adrian J. Matthews
Visualization: Connor Robbins, Adrian J. Matthews
Writing – original draft: Connor Robbins, Adrian J. Matthews
Writing – review & editing: Connor Robbins, Adrian J. Matthews, Rob A. Hall, Ben G. M. Webber, Karen J. Heywood

The MJO has a significant effect on the underlying tropical oceans (DeMott et al., 2015). Primarily, this is through thermodynamical processes that affect the surface mixed layer. Sea surface temperature (SST) anomalies are mainly induced through changes in shortwave radiation flux (through MJO cloudiness anomalies associated with the precipitation) and surface latent heat flux (primarily through changes in wind speed from the MJO surface wind anomalies). A role for the modulation of the surface diurnal warm layer in the ocean has been highlighted (Bernie et al., 2008; Karlowska et al., 2024a). The interaction between the atmosphere and the ocean appears to be, at least weakly, two-way, as coupling an ocean model to the atmosphere can improve MJO forecast skills (Karlowska et al., 2024a; Woolnough et al., 2007), especially if diurnal warm layer processes are well accounted for (Karlowska et al., 2024b).

Dynamical ocean processes in the thermocline play a part in the MJO ocean response. In particular, MJO equatorial zonal wind stress anomalies can force eastward-propagating ocean equatorial Kelvin waves (Hendon et al., 1998; Roundy & Kiladis, 2006). These ocean Kelvin waves can then generate further warm SSTs by advecting warm water eastward and thus feed back onto the atmosphere by triggering atmospheric convection (Kessler et al., 1995). This zonal advection process is most pronounced in the central Pacific; in the eastern Pacific, vertical advection and entrainment are also important in producing variations in SST (McPhaden, 2002). As a result, a sequence of MJO-forced ocean equatorial Kelvin waves in the Pacific basin can help trigger an El Niño event (McPhaden, 1999; McPhaden & Yu, 1999).

The MJO-forced ocean equatorial Kelvin waves in the Indian Ocean can feedback onto the MJO itself. When they reach the eastern boundary, they reflect into ocean equatorial Rossby waves (Webber et al., 2010). These equatorial ocean Rossby waves can trigger or amplify MJO events by producing warm SST anomalies in the western Indian Ocean (Webber, Matthews, et al., 2012; Webber, Stevens, et al., 2012).

There is also a deeper ocean dynamical response to the MJO. Using the then recently available Argo float data in a case study of the December 2003 to February 2004 MJO event, the surface wind anomalies over the equatorial Pacific were shown to trigger an ocean equatorial Kelvin wave response, with coherent observed temperature anomalies down to the limit of the Argo float data at 1,500 m (Matthews et al., 2007). Using the full 3 years of Argo data available at the time, this signal was shown to be reproducible across multiple MJO events, with clear equatorial Kelvin wave signals in temperature and salinity propagating down into the deep Indian and Pacific Oceans (Matthews et al., 2010).

There are now approximately two decades of Argo float data available (Wong et al., 2020) down to a deeper standard operating depth of 2,000 m. Concomitantly, ocean reanalyses are now available that assimilate Argo and other observational data into a dynamically consistent, three-dimensional estimate of the ocean state, typically once per day. These ocean reanalyses contain other dynamical variables that are not directly observed by the Argo system.

In this paper, we diagnose the MJO structure in the deep ocean using 18 years of ocean reanalysis data. Due to the longer time period and dynamical self-consistency that is now available in these data sets, a quantitative analysis of the deep ocean MJO structure is carried out, using two dynamical frameworks (vertical mode framework and a vertically propagating wave framework) to elucidate our understanding of the dynamical mechanisms involved.

2. Data and Methodology

Ocean potential temperature, practical salinity, potential density, and zonal velocity fields were extracted from the GLOBAL_MULTIYEAR_PHY_001_030 product, from the GLORYS12V1 ocean reanalysis (Lellouche et al., 2021). This ocean reanalysis is based on the Nucleus for European Modeling of the Ocean (NEMO) model with data assimilation. An 18-year time period was used, with daily mean fields from 1 January 2003 to 31 December 2020. The data were obtained on 50 vertical levels (with a spacing varying from approximately 1 m near the surface to 300 m at 2,000 m depth), with a horizontal resolution of 1/12°. The data were then regridded to a horizontal resolution of approximately 0.7° (78 km) for ease of computation.

Argo floats form the main observational input to the subsurface ocean and directly measure temperature, salinity (via conductivity), and pressure. Potential density is calculated directly from these variables, and hence the potential density field in the GLORYSV12 reanalysis is directly constrained by the observational input. However, there are very few in situ current observations assimilated into the reanalysis, and therefore the zonal current anomalies shown here are largely model-derived, to be dynamically consistent with the potential density field.

Data were only plotted down to 2,000 m as this corresponds to the maximum depth of regular Argo float measurements.

A basic validation of the zonal current fields in GLORYS12V1 is carried out by comparing with the selected time series of zonal current velocity from the TAO/TRITON and RAMA mooring arrays. Surface wind velocity fields were obtained from the ERA5 reanalysis as hourly data with a horizontal resolution of 1/4° (Hersbach et al., 2020).

To calculate the MJO cycle of a particular variable, anomalies were first created by subtracting the annual cycle, defined here as the time mean plus the first three annual harmonics. The anomalies were then passed through a 20–200-day bandpass filter to isolate the intraseasonal signals, where a wide bandwidth has been deliberately selected because filters with a shorter bandwidth can introduce spurious signals to MJO events and may merge successive events (Matthews, 2000). The state of the MJO on each day was defined using the real-time multivariable MJO (RMM) indices (Wheeler & Hendon, 2004). Composites for a given MJO phase were calculated by averaging the filtered anomaly fields over the days when the RMM indices indicated that the MJO was in that phase and its amplitude was greater than 1.

3. Equatorial Ocean Response to MJO

3.1. Mean State

First, the relevant features of the mean state of the equatorial oceans are shown, so the later MJO anomalies can be put into a spatial context. Over the equatorial eastern Pacific and Atlantic Oceans, the mean surface winds are westward, and these drive westward surface currents (Figure 1a). Ekman divergence at the equator drives the upwelling of colder, denser water, leading to a maximum in surface density along the equator, particularly in the "equatorial cold tongue" of the eastern and central Pacific. The mean surface winds over the Indian Ocean are either eastward or near zero, leading to warm SSTs in the "warm pool" region of the Indian Ocean, Maritime Continent (archipelago of Indonesia and neighboring countries), and western Pacific, indicated by the low-surface density in Figure 1a.

Depth-longitude sections of the equatorial belt (1.5°S–1.5°N; Figures 1b and 1c) show the subsurface extension of these features. The depth axis is split into three (piecewise-linear) sections due to the different thermodynamical and dynamical mechanisms operating there. In the top 50 m (top piecewise linear section), henceforth referred to as the "upper ocean" layer, the potential density in the warm pool is approximately constant with respect to depth (Figure 1b). In the layer below, spanning 50–200 m in depth (middle piecewise linear section), henceforth referred to as the "mid-depth" layer, the potential density increases rapidly with depth, that is, stratification is strong, and this layer corresponds approximately to the thermocline. The third layer represents 200–2,000 m (bottom piecewise linear section), henceforth referred to as the "deeper ocean" layer; in this layer, the potential density increases gradually with depth, and hence stratification is weak.

The equatorial cold tongue of the eastern Pacific is associated with a much shallower thermocline there, such that the thermocline tilts upward toward the east in this region. A similar upward and eastward tilt is observed in the Atlantic. Coincident with the upward and eastward tilting thermocline in the eastern Pacific and Atlantic, there is a strong eastward Equatorial Undercurrent (Figure 1c). Over the Indian Ocean, where there are (weak) eastward winds and downwelling from Ekman convergence on the equator, the thermocline tilts downward toward the east.

We note a slight discontinuity in the thermocline and the Equatorial Undercurrent at 90°W in the eastern Pacific. This is due to the Galapagos archipelago that acts as an equatorial barrier to the zonal flow at this longitude (Karnauskas et al., 2007).

3.2. MJO Cycle

The well-known atmospheric and surface ocean structure of the MJO is now briefly discussed to provide context for the deeper ocean MJO signal to follow. The eastward propagation of the MJO can be seen by the changing position of the red circles in the eight panels of Figure 2. The circles indicate the center of the region of active convection (enhanced rainfall) in each MJO phase; for detailed maps of the spatial structure of these MJO convective anomalies, see, for example, Zhang (2005).

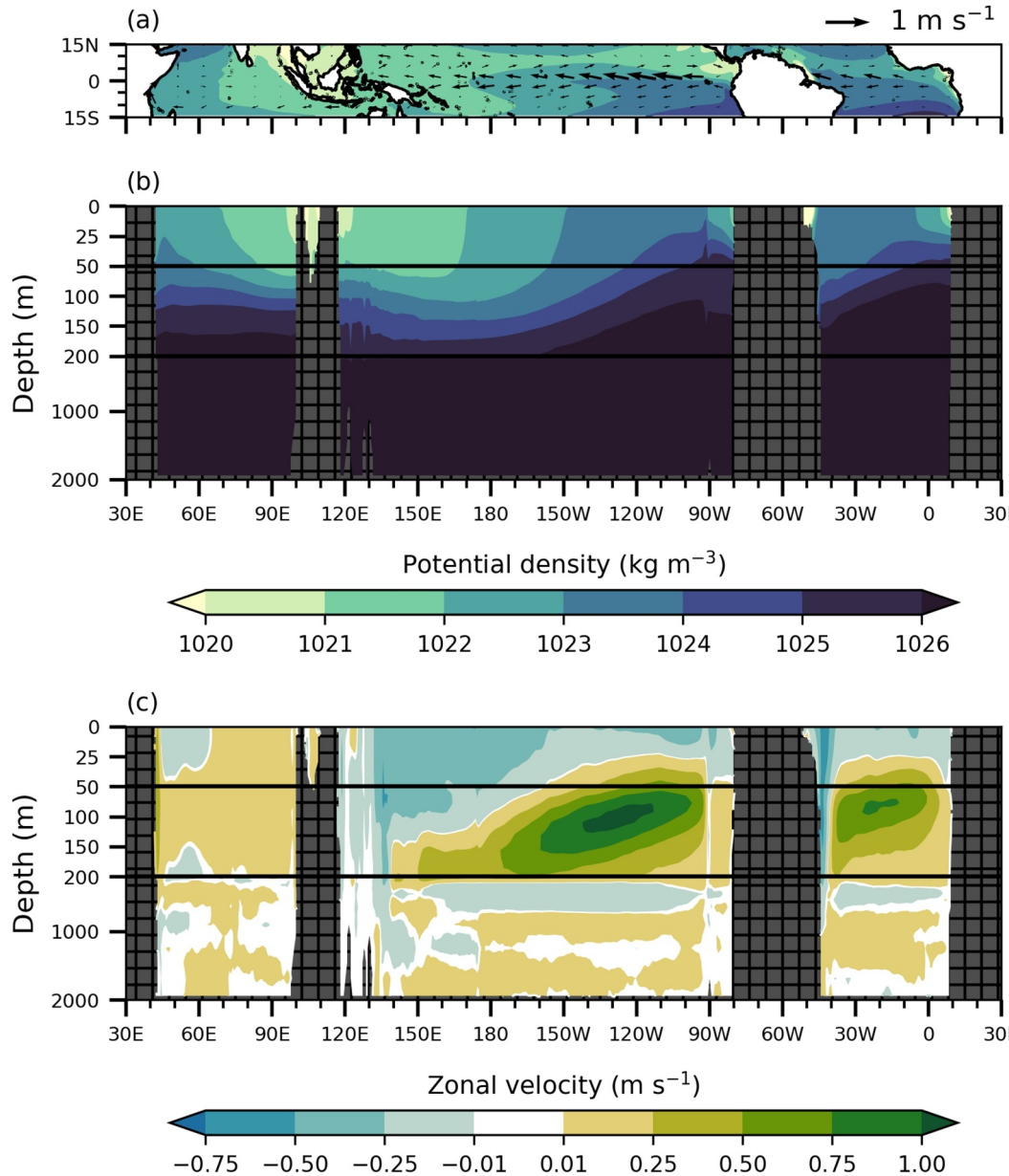

Figure 1. Mean state for the period 2003–2020. (a) Map of ocean surface potential density (shading) and horizontal velocity (vectors). Longitude-depth equatorial (averaged 1.5°S–1.5°N) sections of (b) potential density, and (c) zonal velocity. The depth axis here and in later figures is piecewise linear over three levels: 0–50 m ("upper ocean" layer), 50–200 m ("middepth" ocean layer approximately coincident with the thermocline), and 200–2,000 m ("deeper ocean").

In MJO phase 1, the active convection is located at 70°E in the western Indian Ocean (Figure 2a). This represents the start of a typical MJO event. There are positive SST anomalies across the warm pool region, from the western Indian Ocean through to the western Pacific. As the MJO progresses through phases 2, 3, and 4 (Figures 2b–2d), the convective center moves eastward to the Maritime Continent. The positive SST anomalies precede the MJO convection (i.e., lie to the east), and a region of negative SST anomalies develops behind the MJO convection (i.e., to the west). The surface wind stress vector anomalies show that the MJO active convection is a region of surface convergence, arising from eastward wind anomalies to the west over the Indian Ocean and westward wind anomalies to the east over the Pacific.

MJO phase 5 (Figure 2e) represents a transition phase in terms of oceanic forcing. The positive SST anomalies to the east of the convective center over the eastern Maritime Continent have disappeared, as have the eastward wind

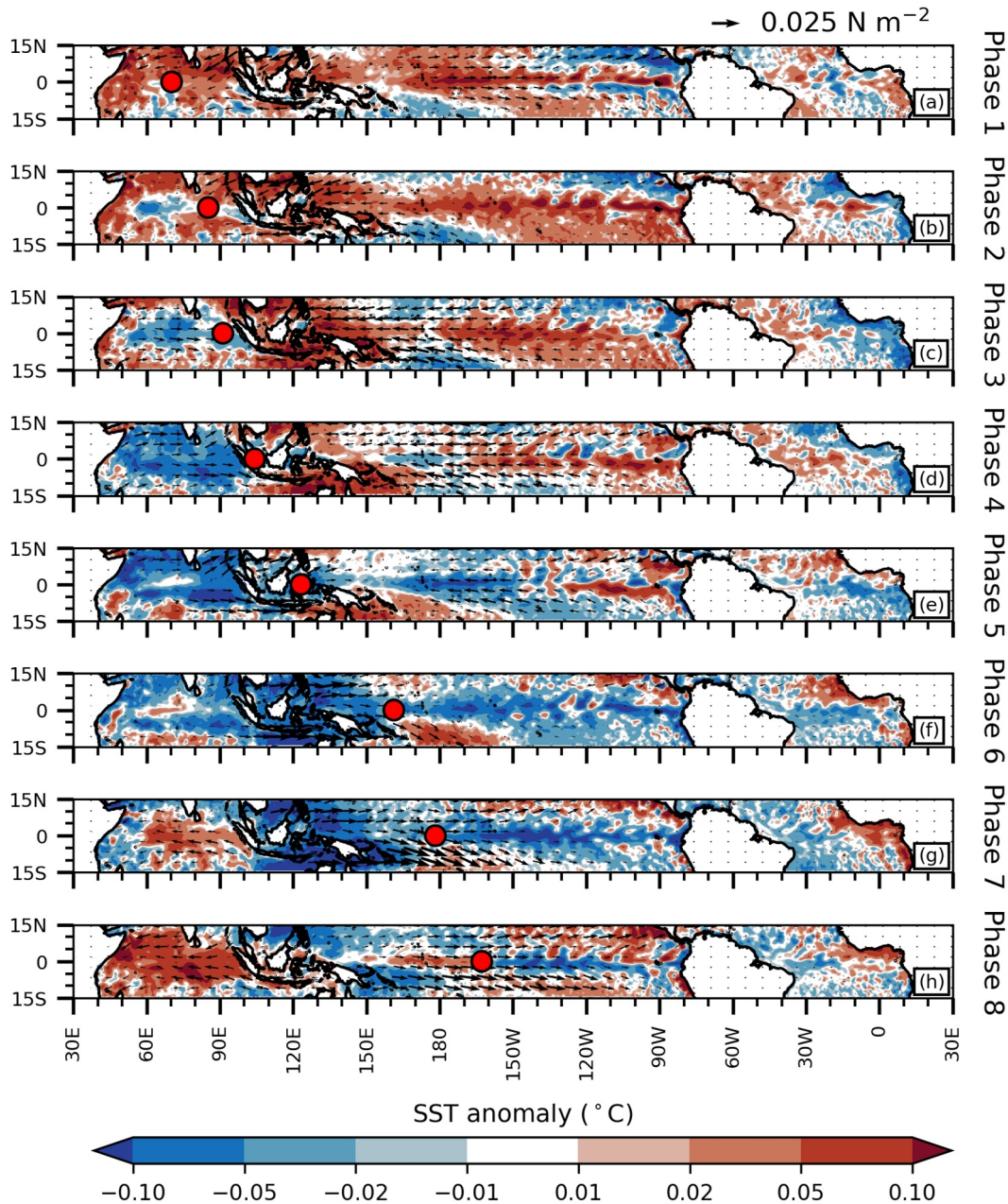

Figure 2. MJO cycle at the ocean surface. Composite anomaly maps for each MJO phase, of sea surface temperature (color shading) and surface wind stress vector. Standard wind stress vector has magnitude 0.025 N m^{-2}. Red circles in each panel show the longitude of the center of the MJO active convection region.

anomalies over the Indian Ocean. There is still a belt of westward wind anomalies over the central Pacific Ocean. During phases 6, 7, and 8 (Figures 2f–2h), the convective center moves into the western and then central Pacific. Positive SST anomalies develop over the Indian Ocean, ahead of the next MJO cycle, along with westward surface wind anomalies there. Eastward surface wind anomalies begin to develop over the western Pacific and spread eastward.

The subsurface continuation of the MJO surface ocean features can be seen in the longitude-depth sections of potential density and zonal velocity along the equator in Figure 3. The overall pattern is one of the anomalies that move eastward with the MJO and extend down from the upper ocean layer into the thermocline and deep ocean. For example, during MJO phase 2, westward surface wind stress anomalies appear over the western equatorial

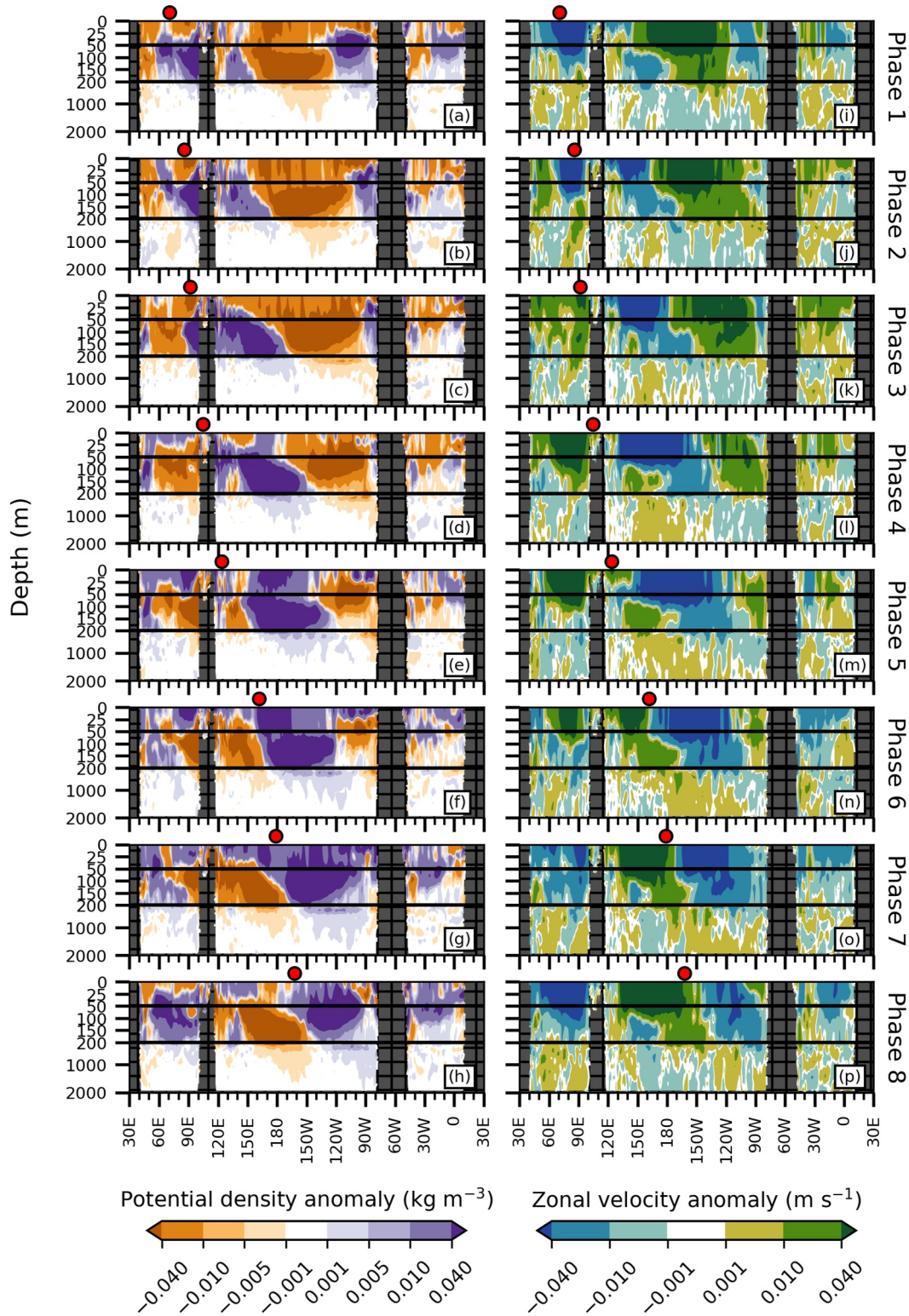

Figure 3. MJO cycle in the equatorial ocean. Longitude-depth sections (averaged 1.5°S–1.5°N) of potential density (left column) and zonal velocity (right column) by the MJO phase (each row). Red circles in each panel show the longitude of the center of the MJO active convection region.

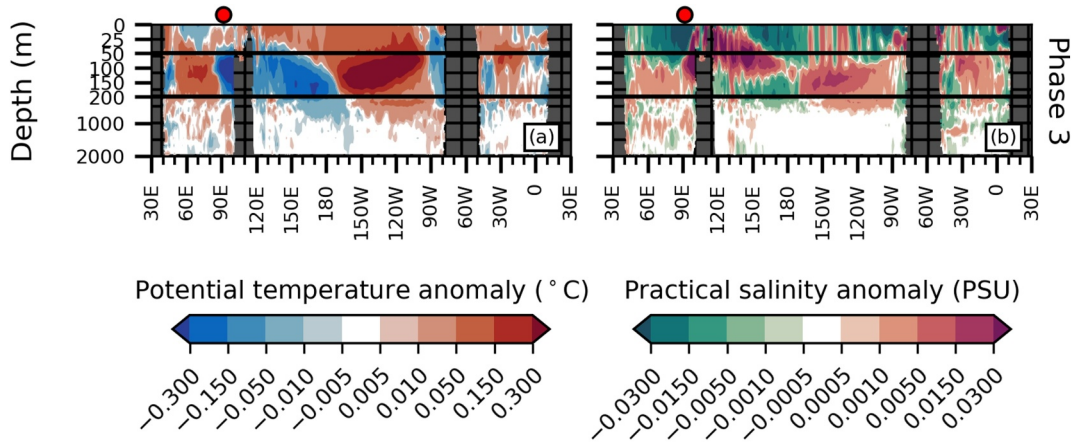

Figure 4. Longitude-depth sections (averaged 1.5°S–1.5°N) of panel (a) potential temperature anomalies (b) practical salinity anomalies, for MJO phase 3. Red circles in each panel show the longitude of the center of the MJO active convection region.

Pacific (Figure 2b). Through Ekman divergence, this triggers an upwelling equatorial Kelvin wave, manifested as positive potential density anomalies in the thermocline in this region (Figure 3b). These positive potential density anomalies in the thermocline strengthen and move eastward into the central Pacific during MJO phases 3–6 (Figures 3c–3f), reaching the eastern Pacific in phases 7–8 (Figures 3g and 3h).

In MJO phase 6, the westward surface wind stress anomalies over the western Pacific are replaced by eastward anomalies (Figure 2f). These induce Ekman convergence and a downwelling equatorial Kelvin wave such that negative potential density anomalies appear in the thermocline here (Figure 3f). These negative potential density anomalies then propagate eastward, reaching the central Pacific by MJO phase 8 (Figure 3h). The potential density anomalies of both signs also extend down into the deeper ocean, below 200 m, and also exhibit a distinctive vertical tilt downward and eastward (Figures 3f–3h). Note that, here, we have focused on MJO phases 2 and 6 as examples, but the MJO continues to force Kelvin waves further east in the Pacific in later MJO phases.

In the Indian Ocean, the eastward wind stress anomalies in MJO phase 3 (Figure 2c) force downwelling and negative potential density anomalies in the thermocline that propagate eastward to the Sumatran coastline on the eastern boundary during MJO phases 3–7 (Figures 3c–3g). In the Atlantic, the MJO wind stress anomalies are very weak (Figure 2) and no coherent subsurface signal arises (Figure 3). Further discussion on the MJO surface wind signal in the equatorial Atlantic can be found in Foltz and McPhaden (2004).

The dynamic upper-ocean response to the MJO is known to feed back onto atmospheric intraseasonal variability, influencing the initiation and propagation of the MJO (Rydbeck et al., 2017; Rydbeck & Jensen, 2017; Webber et al., 2010; Webber, Matthews, et al., 2012). Here, we focus on the deep ocean response to the MJO, which has received less attention.

We focus on potential density as the key thermodynamical variable in this study, as it is potential density that determines stratification and wave properties. Nonetheless, it is informative to put the potential density anomalies for a sample MJO phase 3 (Figure 3c) in the thermocline and deeper ocean in the context of the potential temperature (Figure 4a) and practical salinity (Figure 4b) anomalies that might be observed for the same MJO phase. For example, the positive potential density anomaly of 0.088 kg m^{-3} at 155 m depth at 180°E is associated with a negative potential temperature anomaly of −0.32°C and a negative practical salinity anomaly of −0.0083. These are both associated with upwelling as the mean temperature and salinity vertical gradients are both positive at this location. The contributions to the potential density are of the opposite sign: positive from temperature and negative from salinity, with the temperature contribution strongly dominating.

A basic check is first carried out on the GLORYS12V1 current fields by comparing them to selected time series of observed zonal current velocity from equatorial moorings in the TAO/TRITON and RAMA arrays. Intraseasonal (20–200-day filtered) currents from GLORYS12V1 are similar in phasing and magnitude to the observed mooring data (Figure S1 in Supporting Information S1), validating the use of these data here. Additionally, a good

general agreement has been found between GLORYS12V1 current data and observed currents from drifters in the tropical Pacific (Lellouche et al., 2021).

The MJO zonal velocity anomalies are dynamically consistent with the potential density anomalies, as expected due to the assimilation system of the GLORYSV12 reanalysis. Hence, the upwelling equatorial Kelvin wave, triggered in the western Pacific at MJO phase 2 that then propagates to the eastern Pacific by phase 8, has associated westward (negative) zonal velocity anomalies (Figures 3k–3p). Similarly, the downwelling equatorial Kelvin wave initiated over the western Pacific in MJO phase 6 has eastward (positive) zonal velocity anomalies associated with it. These zonal velocity anomalies also extend down into the deeper ocean and have the same characteristic downward and eastward phase tilt that was noted for the density field (Figures 3f–3h and 3n–3p). Previous studies using moored velocity data from the Pacific (Kutsuwada & McPhaden, 2002) and Indian (Iskandar & McPhaden, 2011) oceans have found upward phase propagation of intraseasonal Kelvin waves consistent with downward energy propagation into the thermocline.

In the following sections, the deep vertical structure is investigated further and interpreted within two theoretical frameworks: vertical modes and vertically propagating waves.

4. Vertical Mode Framework

4.1. Modal Structures

The subsurface ocean structure of the MJO has been generally interpreted in terms of the dynamical "vertical modes" that a stratified ocean supports (Hendon et al., 1998; Matthews et al., 2007, 2010; Pujiana & McPhaden, 2020). These vertical modes are eigenfunctions of the vertical structure equation that arises when a separable solution is sought to the equations of motion. The resulting full solution for, for example, the potential density $\sigma'(x,y,z,t)$ is in the form of a latitudinal structure $\hat{\sigma}(y)$ multiplied by an eastward- or westward-propagating wave $\cos\left[k(x-ct)-\phi_0\right]$, further multiplied by a vertical mode structure $f(z)$:

$$\sigma'(x,y,z,t) = \hat{\sigma}(y)\cos\left[k(x-ct)-\phi_0\right]f(z). \quad (1)$$

here, x, y and z are distance eastward, northward, and upward, respectively, t is time, k is the zonal wavenumber, c is the eastward phase speed, and ϕ_0 is a phase offset. The horizontal and time-dependent (x,y,t) parts of the solution lead to the shallow water equations, of which the relevant solution here is that of equatorial Kelvin waves. We apply this vertical mode framework here.

The vertical modes were calculated using the Dynmodes package (downloaded from https://www.eoas.ubc.ca/~sallen/AIMS-workshop/_modules/dynmodes.html). The input to this is a vertical profile of the stratification [buoyancy frequency squared $N^2(z)$]. This was calculated from the 18-year time-mean vertical profiles of potential temperature and practical salinity from the GLORYS12V1 reanalysis, averaged over the equatorial belt (1.5°S–1.5°N), and extending over the full depth of the ocean from the surface to the ocean floor. The modes were calculated independently at each longitude, as the mean state stratification varies considerably across the ocean basins (Figure 1b).

The structures of the first three vertical modes are shown for a sample longitude (149.8°E) in the warm pool region of the western Pacific (Figures 5a–5c). It should be noted that this analysis assumes the background ocean to be at rest. However, particularly in the Pacific, strong equatorial undercurrents will affect the vertical structure of intraseasonal Kelvin waves and, as such, the presented structures are an idealization of the true observed vertical structure (Johnson & McPhaden, 1993; McPhaden et al., 1987). The normalization is such that the horizontal velocity structures are dimensionless. As a consequence, the potential density structures have dimensions of inverse time.

As expected, Mode 1 has one crossing point in its velocity structure, near 1,000 m depth (blue line in Figure 5c), and is single-signed in its potential density structure (blue line in Figure 5a). Hence, Mode 1 effectively has a two-layer structure, with a layer of, for example, eastward flow above a layer of westward flow. Mode 2 has two crossing points in its velocity structure (orange line in Figure 5c) and one crossing point in its potential density structure (orange line in Figure 5a). It therefore represents a three-layer structure with a sandwich of, for example, westward-eastward-westward layers. Mode 3 (green lines) has one extra crossing point and represents a four-

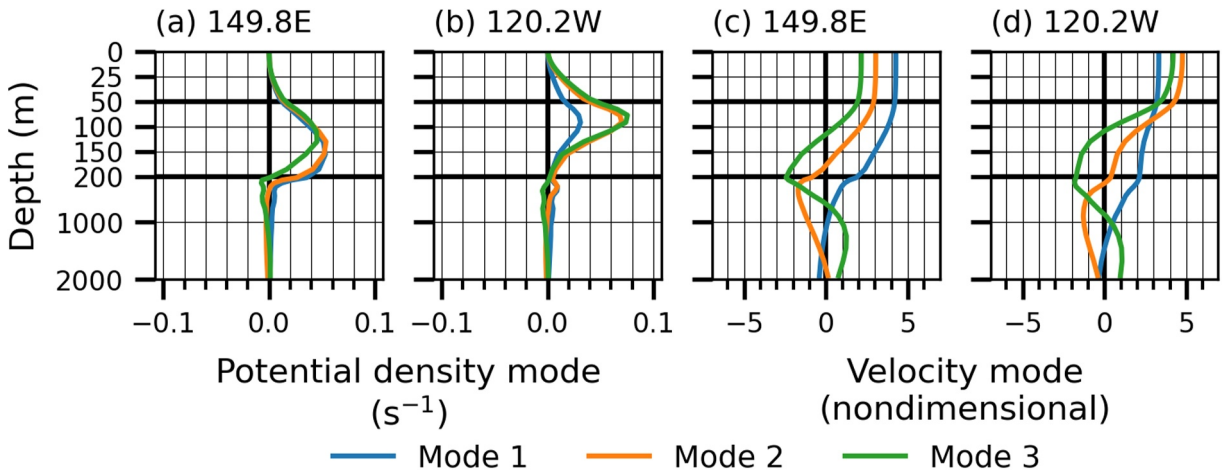

Figure 5. Vertical structures of the first three normal modes of the vertical structure equations at two sample longitudes: 149.8°E in the western Pacific, with potential density in panel (a) and horizontal velocity in panel (c); and 120.2°W in the eastern Pacific, with potential density in panel (b) and horizontal velocity in panel (d). The structures are only shown down to 2,000 m.

layer structure of, for example, westward-eastward-westward-eastward layers. Note that the final crossing point of Mode 3 is below 2,000 m (the cutoff in Figure 5).

Each higher mode (Mode 4, Mode 5, etc., not shown) will have one extra crossing point. The main features of all the modes are concentrated in the thermocline region, where the stratification is largest (Figure 1b). The structures of the first three modes are shown for a further sample longitude (120.2°W) in the equatorial cold tongue region of the eastern Pacific (Figures 5b–5d). The modal structures are similar to those in the western Pacific, but the main features are all at a shallower depth, consistent with the shallower thermocline in the eastern Pacific.

4.2. Vertical Mode Amplitude Changes Through MJO Cycle

As noted in Section 4.1, oceanic equatorial Kelvin waves associated with the MJO have been generally interpreted in this vertical mode framework. An implicit assumption is that one mode, or, at most, a small number of modes, will essentially describe the variability observed. In this section, the amplitude of each vertical mode along the equator is ascertained to test this assumption.

The vertical modes are eigenfunctions of the vertical structure equation. Therefore, they form a complete set of modes, and any arbitrary potential density profile or zonal velocity profile can be expressed as a weighted superposition of the relevant mode structures at that longitude (e.g., Figures 5a–5c). The weighting for a particular mode can be viewed as its amplitude at that location. This approach is used to decompose the MJO anomalies of potential density and zonal velocity into their vertical modes. Hence, for each MJO phase, at each longitude, the profiles of potential density anomaly and zonal velocity anomaly are used to calculate the amplitudes of the respective vertical modes. The purpose of this decomposition is that if only a very small number (one, or possibly two) of the vertical modes have a significant amplitude, and the amplitude of all the other modes is small, then the deep ocean MJO structure can be said to be essentially determined by these one or two modes, whose dynamics are known, thus providing a theoretical understanding of the ocean response to the MJO.

The results of this decomposition are shown for two sample MJO phases (Phases 3 and 5; Figure 6). In the western Pacific during MJO phase 3, the potential density anomalies are positive in the thermocline depth range (50–200 m; Figure 3c). The potential density modal structures are positive in the western Pacific in this depth range for Modes 1, 2, and 3 (Figure 5a). Hence, the amplitudes of these first three modes are all positive in this region during MJO phase 3 (Figure 6a).

In the eastern Pacific, the potential density anomalies are negative in the thermocline (Figure 3c). The potential density modal structures are still all positive in the eastern Pacific in this depth range for Modes 1, 2, and 3 (Figure 5b). Hence, the amplitudes of these first three modes are all negative in this region during MJO phase 3 (Figure 6a).

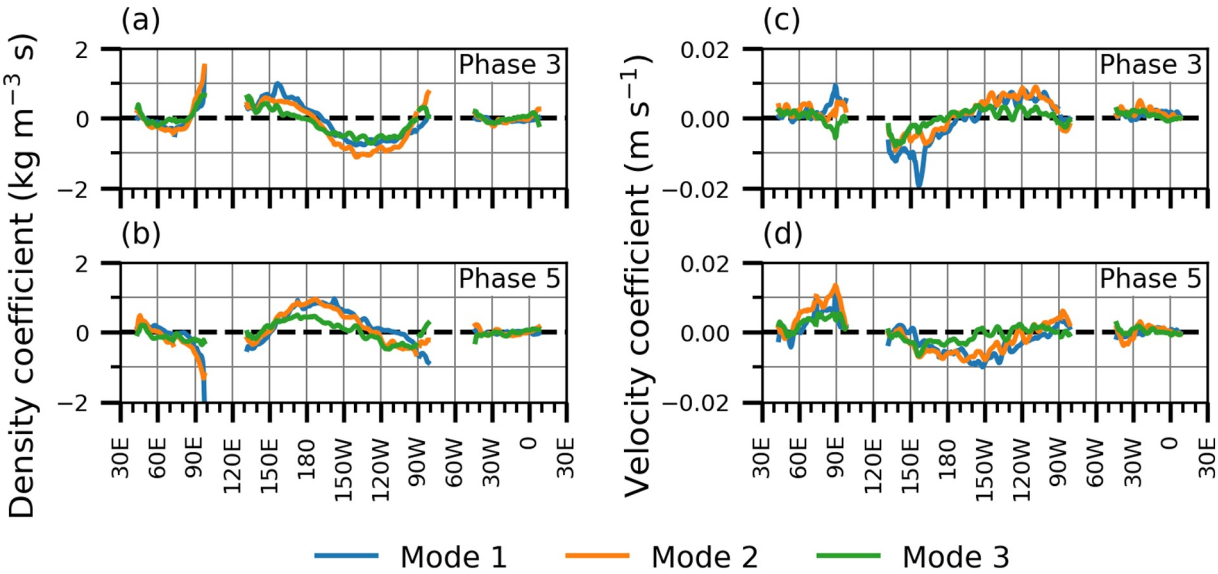

Figure 6. Longitudinal variation of dimensional coefficients of the first three normal modes for the selected MJO phases. Potential density in MJO phases 3 (a) and 5 (b). Horizontal velocity in MJO phases 3 (c) and 5 (d).

Similarly, the zonal velocity anomalies in the western Pacific in MJO phase 3 are negative (westward) near the surface, transitioning to weakly positive below (Figure 3k). The zonal velocity modal structures are all positive in the western Pacific near the surface for Modes 1, 2, and 3 (Figure 5c). This leads to the amplitudes of these first three modes being all negative in this region during MJO phase 3 (Figure 6c). In the eastern Pacific, the MJO zonal velocity anomalies change to being positive near the surface (Figure 3k), leading to the amplitudes of the first three modes being all positive in this region during MJO phase 3 (Figure 6c).

A quarter cycle later, in MJO phase 5, the ocean anomalies have shifted eastward (Figures 3e–3m). In a consistent manner, the envelopes of the mode amplitudes have also shifted further east in the Pacific (Figures 6b–6d). We note in general that the Mode 1 and mode 2 amplitudes tend to be stronger than the Mode 3 amplitudes in Figure 6. However, there is no obvious single mode that stands out above the others.

To further explore the usefulness of the vertical mode framework, the MJO anomalies in potential density and zonal velocity are reconstructed by an amplitude-weighted superposition of the first three vertical modes (Figures 7a–7c). These reconstructions do capture the major features of the corresponding MJO phase 3 anomalies (Figures 3c–3k), but there are many features that are not captured, in particular the eastward and downward tilt to the potential density anomalies. It is only when a reconstruction using the first 10 vertical modes is created (Figures 7b–7d) that these tilts are reproduced. A similar number of vertical modes was needed to reproduce the structure of the equatorial intermediate current in the Indian Ocean (Huang et al., 2018).

However, the inability to capture the vertical tilts in the deeper ocean, unless up to 10 vertical modes are included, does raise a question as to how useful the modal analysis is in providing a clean dynamical description of the ocean dynamical processes involved. As the vertical modes mathematically form a complete basis set of eigenfunctions, then by definition, as more modes are included, the resulting reconstruction will more accurately reproduce the observed anomalies. However, this does not infer a physically useful role for such an analysis.

Note that even when 10 vertical modes are used for the reconstruction, the MJO anomalies of potential density in the upper ocean layer are not reproduced. However, this is to be expected as MJO air-sea fluxes or other oceanic processes, that are unrelated to Kelvin waves, can strongly influence the variability within the upper ocean layer (Chi et al., 2014).

4.3. Meridional Structure

The usefulness of the vertical mode framework in explaining the MJO dynamical ocean anomalies can be further explored by examining the meridional structure of the anomalies, for example, for MJO phase 3 at the sample

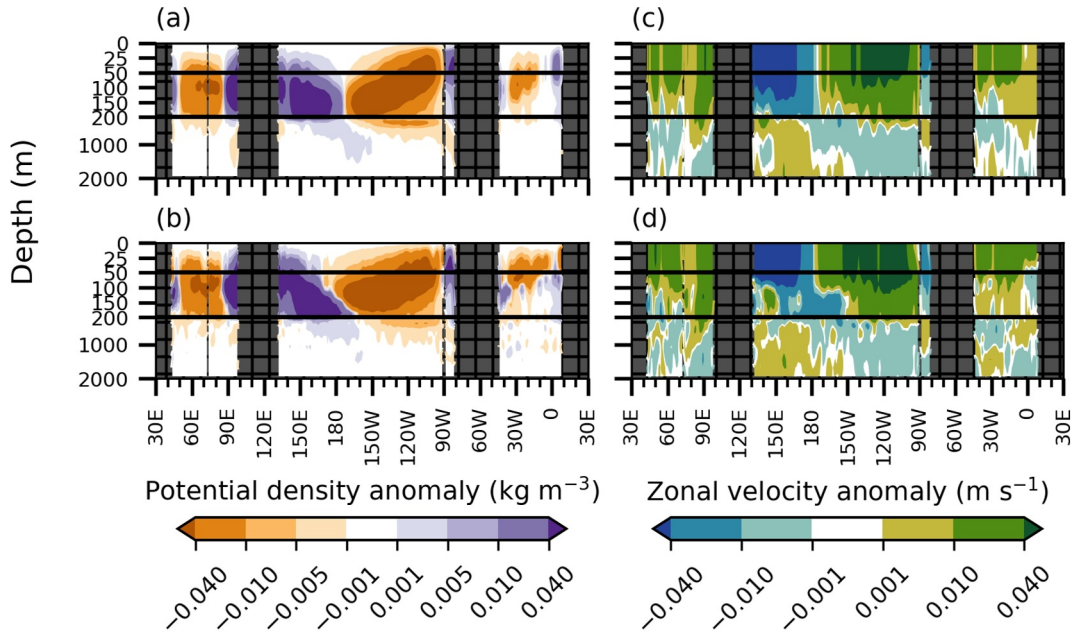

Figure 7. Reconstruction of MJO phase 3 anomalies from normal mode decomposition. Potential density anomalies using the first three modes (a) and 10 modes (b). Zonal velocity anomalies using three modes (c) and 10 modes (d).

longitude of 149.8°E in the western Pacific (Figure 8a). Here, the positive potential density anomaly at the equator in the thermocline region already noted in Figure 3c can be seen to be part of a meridional structure that is a maximum at the equator and decays in strength to the north and south with a trapping scale of a few degrees.

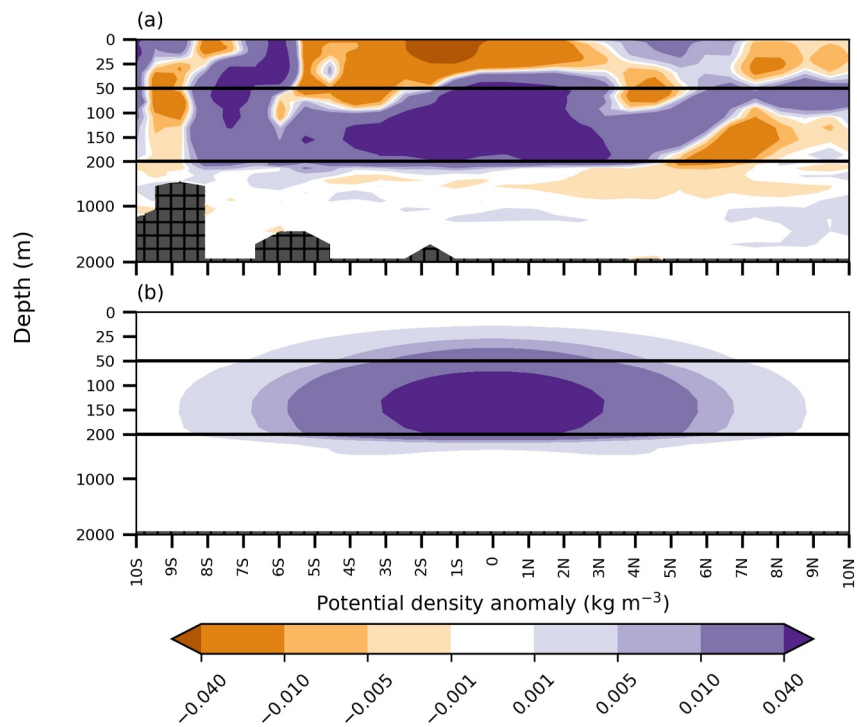

Figure 8. Latitude-depth sections for MJO phase 3 at 149.8°E. (a) Composite potential density anomalies. (b) Reconstruction of potential density using first three modes and associated length scales.

This is consistent with a theoretical equatorial Kelvin wave structure, where the latitudinal structure of Equation 1 has a Gaussian structure given by

$$\hat{\sigma}(y) = \sigma_0 e^{-\beta y^2/2c} = \sigma_0 e^{-(y/y_0)^2} \quad (2)$$

where σ_0 is a constant (the amplitude of the function), $\beta = df/dy$ is the northward gradient of planetary vorticity, c is the eastward phase speed of the relevant vertical mode (from Equation 1), and $y_0 = \sqrt{2c/\beta}$ is the trapping scale for the Gaussian structure.

Each vertical mode number has an associated phase speed c, which is calculated by the Dynmodes package. The phase speeds of Modes 1, 2, and 3 are 2.1–3.2, 1.1–2.1, and 0.8–1.4 m s^{-1}, respectively. The range of values is because the background stratification, and therefore the mode speed, depends on longitude. The higher values are found in the central Pacific and the lower values in the eastern Pacific. This longitudinal dependence in the Pacific is consistent with observed phase speeds of Kelvin waves (Rydbeck et al., 2019).

For the sample longitude of 149.8°E shown here, the phase speeds of the first three modes are 3.0, 1.8, and 1.1 m s^{-1}, corresponding to Gaussian trapping scales of 510, 400, and 310 km, respectively. The best-fit Gaussian structure to the observed anomalies in Figure 8a at a depth of 150 m yields a trapping scale of 465 km and a phase speed of 2.5 m s^{-1}. The vertical profiles from the first three vertical modes are then combined with their theoretical Gaussian latitudinal structures to produce a reconstructed latitudinal section of the combined modal structure at 149.8°E in MJO phase 3 (Figure 8b). This does a reasonable job of reproducing the observed latitudinal structure in Figure 8a, in terms of the vertical and horizontal extent of the positive potential density anomalies. Hence, the vertical mode framework is reasonably successful in accounting for the MJO structure in the thermocline, but as we saw in Section 4.2, it is found wanting in accounting for the MJO structure in the deeper ocean.

4.4. Forced and Free Ocean Kelvin Wave Propagation

4.4.1. Response of Individual Vertical Modes

As noted in Section 4.3, the different vertical modes have different horizontal phase speeds c. Hence, an examination of the apparent observed phase speeds of each vertical mode can give further insights into the applicability of the vertical mode framework in understanding MJO ocean dynamics.

A "time"-longitude diagram of the observed MJO equatorial zonal wind stress anomalies (black line contours in Figure 9a) indicates the evolution of the forcing of oceanic equatorial Kelvin waves during the MJO cycle. Note that the vertical "time" axis is actually the MJO phase. Assuming a 7-day average residence time for each of the 8 MJO phases, this leads to the time axis being 56 days in length. This is consistent with previous work, for example, Hendon et al. (1998), which found that the lower frequency end of the approximate 30–60-day period atmospheric MJO forcing is most effective at forcing a dynamical ocean response. However, we note that climate change-induced warming is warping the MJO cycle and the length of each phase, particularly in the Indo-Pacific region (Roxy et al., 2019).

In MJO phase 1, there are negative (westward) zonal wind stress anomalies over the Indian Ocean and western Pacific and positive (eastward) zonal wind stress anomalies over the central and eastern Pacific. During MJO phases 2 and 3, the region of negative zonal wind stress anomaly propagates slowly eastward at an estimated speed of 5 m s^{-1}. In MJO phase 4, the region of westward zonal wind stress anomalies reaches the central Pacific, where it speeds up (estimated speed of 25 m s^{-1}) and rapidly crosses the entire Pacific to the coast of South America. During MJO phases 5–8, a similar behavior emerges, but with a region of *eastward* zonal wind stress first propagating slowly eastward over the western Pacific, then rapidly across the central and eastern Pacific. This behavior has been previously ascribed to the atmospheric part of the MJO, with a slow eastward propagation over the warm pool region of a dynamical atmospheric MJO system coupled to moist atmospheric convection, followed by a rapid eastward propagation over the central and eastern Pacific of a "dry" atmospheric equatorial Kelvin wave, uncoupled from moist convection (Matthews et al., 1999).

At the western Pacific boundary, the negative (westward) zonal wind stress anomalies clearly force a positive amplitude ocean Kelvin wave Mode 1 (Figure 9a). This is consistent, as westward zonal wind stress on the equator

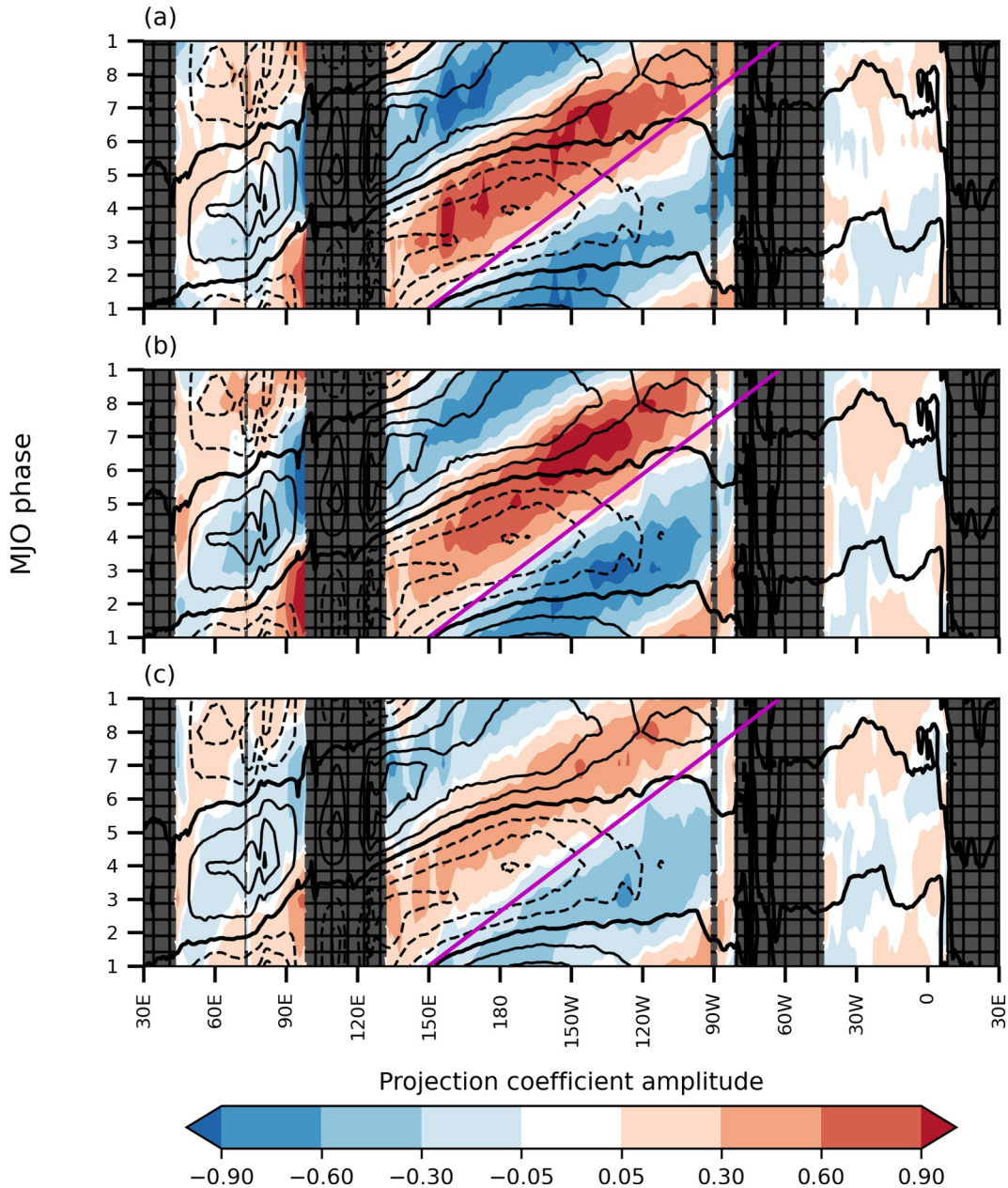

Figure 9. "Time"-longitude diagrams of the amplitude of the (a) first, (b) second, and (c) third density modes (color shaded). The vertical axis is the MJO phase, analogous to a time axis. The equatorial (averaged 5°S–5°N) surface zonal wind stress anomaly is line contoured with interval 5×10^{-3} N m^{-2}; the zero contour is shown by a thick solid line, positive contours are solid, and negative contours are dashed. The magenta line represents a velocity of 3.4 m s^{-1}, assuming a time period of 56 days for the MJO cycle.

leads to Ekman divergence and upwelling, bringing up high density water from below. The Mode 1 density structure has a positive density anomaly in the thermocline (Figure 5a); hence, forced upwelling will lead to a positive amplitude for this mode.

This positive Mode 1 structure then propagates eastward with a phase speed of approximately 3.4 m s^{-1} (this value, calculated by a linear fit to the observed propagation of Mode 1 potential density anomalies, is indicated by the magenta lines in Figures 9 and 10). This is similar to, but slightly higher than, the theoretical (intrinsic) eastward phase speed of this mode calculated using Dynmodes and the local hydrography (varies between 2.1 and 3.2 m s^{-1}, depending on longitude). Hence, it appears that ocean Kelvin wave Mode 1 is efficiently forced by the

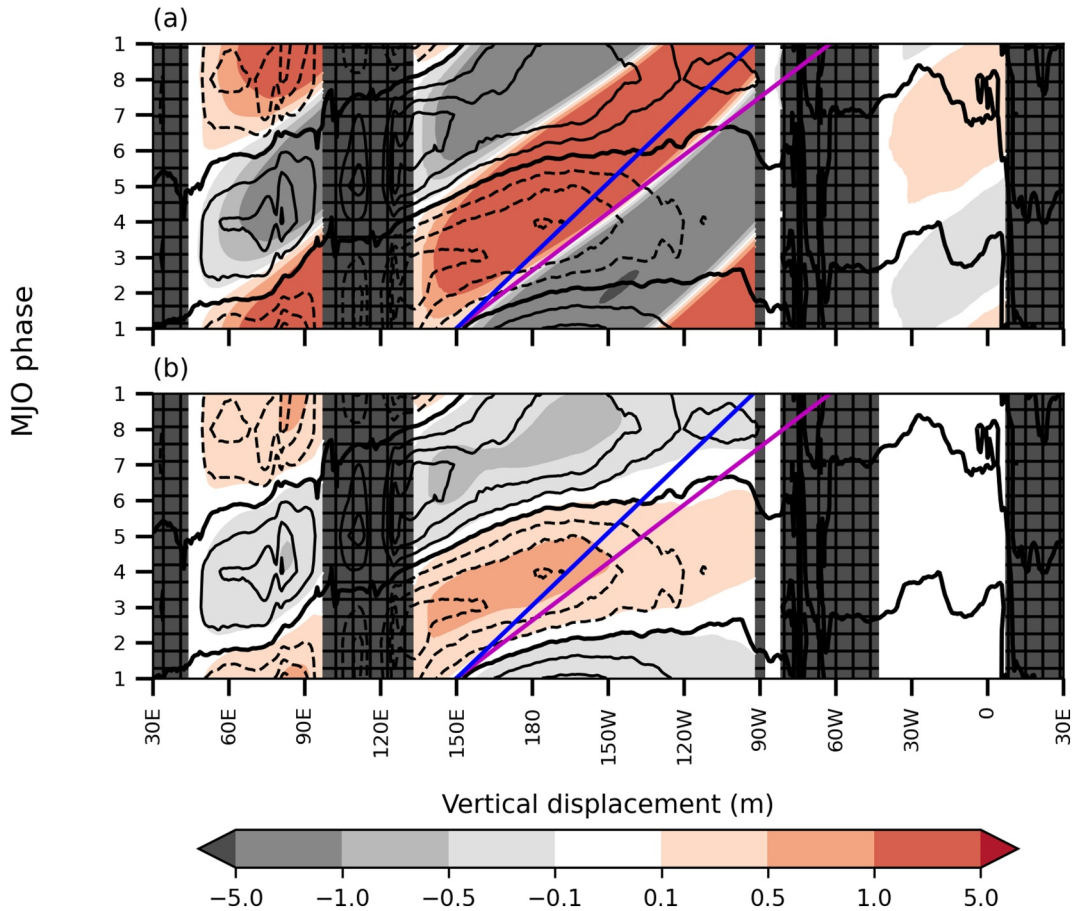

Figure 10. Vertical displacement of the equatorial Kelvin wave response to observed anomalous equatorial MJO wind stress forcing (line contours), assuming a Kelvin wave speed of 2.7 m s^{-1}. Decay factors of panel (a) $\lambda = 0$, (b) $\lambda = 0.3$ day^{-1}. Wind stress conventions are as in Figure 9. The blue and magenta lines represent velocities of 2.7 and 3.4 m s^{-1}, respectively.

MJO wind stress anomalies and then propagates eastward across the Pacific basin, but at a phase speed slightly faster than its theoretical speed.

Similarly, in the second half of the MJO cycle, the positive (eastward) zonal wind stress anomalies on the western boundary of the Pacific force a downwelling, negative amplitude Mode 1 ocean Kelvin wave that also propagates eastward at 3.4 m s^{-1}, slightly faster than its intrinsic speed. In the Pacific, the equatorial undercurrent provides a strong nonzero mean flow which leads to Doppler shifting and alters the observed phase speeds. As such, slightly higher phase speeds would be expected here (McPhaden et al., 1987; McPhaden & Ripa, 1990). In the Indian Ocean, the Mode 1 response is consistent with the MJO zonal wind stress forcing. In the Atlantic, the wind stress forcing is extremely weak, and consequently the Mode 1 response is also very weak.

Surprisingly, the Mode 2 and Mode 3 responses (Figures 9b and 9c) look very similar to each other and to the Mode 1 response, even though the Mode 2 and Mode 3 intrinsic phase speeds are much slower (1.1–2.1 and 0.8–1.4 m s^{-1}, respectively). All three modes propagate eastward across the Pacific in synchrony with each other despite their very different phase speeds, which implies that the modal framework may not be straightforward in helping us to understand these MJO ocean dynamics. The likely explanation is that the MJO wind forcing projects mainly onto Mode 1. However, other factors then interfere, such as the change in background stratification across the Pacific (Figure 1b) and the nonzero mean state flow (Figure 1c). These can cause energy to transfer out of the theoretical Mode 1 structure and into the higher modes (Cravatte et al., 2003). Vertical propagation of waves, which will be discussed in Section 5, can cause the Mode 1 waves to project onto higher mode vertical structures, thus creating an apparent signal in Modes 2 and 3. In the next section, we use a model to test how wind forcing can alter the phase speed of forced Kelvin waves from the theoretical modal wave speed.

4.4.2. A Simple Wave Response Model

A simple model was run to assess the response of the thermocline to the observed MJO zonal wind stress forcing by eastward propagating waves with a fixed phase speed of $c = 2.7$ m s^{-1}, representing the average phase speed of the Mode 1 ocean Kelvin wave (Chelton et al., 1998). The amplitude of the wave response is assumed to decay exponentially with the damping scale λ. The forcing $F(x,t)$ is taken as the time-longitude zonal wind stress anomalies shown by the black contours in Figure 9. The forcing is cyclical in time, with period 56 days. Waves are assumed to be absorbed completely when they reach the eastern boundary; therefore, each ocean basin is effectively considered separately. In this model, the total response $R(x,t)$ of the thermocline depth is a superposition of the responses to all forcings at previous times, allowing for wave propagation and damping. It can be written as a convolution

$$R(x,t) = \alpha \int_{-\infty}^{t} F(x - ct', t')\, \mathrm{e}^{-\lambda t'}\, \mathrm{d}t', \tag{3}$$

where $\alpha = 13$ m^3 kg^{-1} is a scaling constant chosen to approximate the equatorial upwelling in m d^{-1} generated by a Gaussian wind patch with the maximum wind stress of 1 N m^{-2}, where the equatorial Ekman upwelling is calculated by including a frictional coefficient, $\epsilon = 1$ d^{-1}, following Xie (2024). This model is analogous to that used by Kessler and McPhaden (1995) to explain variability in the thermocline at 140°W during the 1991–1993 El Niño; however, their model was written as an integral with respect to x and therefore used a different scaling coefficient. The model is run for two cases, one without damping and one with high damping (Figure 10).

The undamped wave response ($\lambda = 0$) is shown in Figure 10a. In the Pacific, the strongest forcing is near the western boundary and this elicits a strong wave response there. An upwelling wave is forced by the negative (westward) wind stress forcing over the western Pacific in MJO phases 1–4, and a downwelling wave is forced by the positive (eastward) wind stress forcing in MJO phases 5–8. This strong undamped response propagates eastward as free waves and overwhelms the weaker response to the weaker forcing over the eastern Pacific. Overall, this simple wave propagation model matches the observed response in Figure 9 reasonably well. The magenta line indicates a phase speed of 3.4 m s^{-1} for comparison with the observations of Figure 9. Furthermore, our simulation shows that the forced wave responses propagate at approximately this faster phase speed of 3.4 m s^{-1} across the western and central Pacific, where the forcing is strong, but propagate closer to the free wave phase speed of 2.7 m s^{-1} (blue line in Figure 10a) in the eastern Pacific where the local wind stress anomalies are weak. This demonstrates that the forced wave propagation speed can be significantly faster than the free propagation speed.

In contrast, a very strongly damped wave response ($\lambda = 0.3$ day^{-1}) is shown in Figure 10b. The strongly damped waves do not propagate significantly before being dissipated, and, consequently, the response closely follows the forcing, with a phase speed much higher than the observed 3.4 m s^{-1}. This is not a good fit for observations. This experiment demonstrates that the rate at which the Kelvin wave energy radiates into the deep ocean and decays in the thermocline can affect both the amplitude and apparent phase speed of the forced response. Experiments with lower damping rates only become realistic at small values of λ, at which point the simulations appear very similar to Figure 10a (not shown), suggesting that this damping rate is low in the observations.

The idealized model calculations presented here demonstrate that the equatorial dynamic ocean response to MJO forcing can be represented as the sum of continuously forced ocean Kelvin waves, with a free propagation speed of approximately 2.7 m s^{-1}, but with an apparent propagation speed that is faster (closer to 3.4 m s^{-1}) due to the relatively fast (>5 m s^{-1}) atmospheric propagation speed of the wind stress anomalies.

5. Vertical Wave Propagation Framework

The vertical mode framework has proven partially satisfactory in interpreting the MJO ocean dynamical signal. However, no single vertical mode (or very small number of vertical modes) was able to account for all the observed features, in particular, the eastward and downward tilts in the anomalies in the deep ocean.

In this section, an alternative framework is investigated, that of vertical propagation of plane waves. Instead of purely horizontally propagating waves with fixed vertical structures (the vertical mode framework), this framework assumes a forcing region at the surface, which then triggers waves that freely propagate eastward and

downward as plane waves. Further discussion on these two frameworks for oceanic equatorial waves can be found in Philander (1978). Phase lines will tilt downward and eastward, for a wave that is forced near the ocean surface and whose energy is propagating downward into the deep ocean (Holton & Hakim, 2012).

The potential density anomalies in Figure 3 have low amplitude in the deep ocean (below the thermocline), compared with those in the thermocline. This can be understood as a consequence of vertical motion within layers of differing stratification. The implied vertical displacement ξ of a water parcel can be calculated as

$$\xi = -\sigma' \Big/ \left(\frac{\mathrm{d}\sigma_{\mathrm{ref}}}{\mathrm{d}z}\right), \tag{4}$$

where σ' is the potential density anomaly of the water parcel, and $\mathrm{d}\sigma_{\mathrm{ref}}/\mathrm{d}z$ is the vertical gradient of the mean state potential density. Hence, in the deep ocean, where the stratification $\mathrm{d}\sigma_{\mathrm{ref}}/\mathrm{d}z$ is weak, then for a given vertical displacement from a passing wave, the resulting potential density anomaly will be weaker than in the thermocline, where the stratification is large.

The MJO potential density anomalies (Figure 3) are converted to implied vertical displacements (Figure 11) using Equation 4 with the time-mean potential density profiles at each longitude. The penetration of the MJO signal into the deep ocean can be clearly seen, with significant vertical displacements right down to 2,000 m, the maximum depth of the Argo observational network. In particular, the clear downward and eastward phase lines of the response are visible. This is consistent with a theoretical downward-propagating equatorial Kelvin wave.

Ray paths for eastward and downward-propagating Kelvin waves can be constructed (Amol et al., 2022; McCreary, 1984). A ray path, emanating from a point (x_0, z_0), is the set of points $\{(x, z = S(x))\}$ found by integrating

$$\frac{\mathrm{d}S}{\mathrm{d}x} = \sqrt{\frac{\omega^2}{N^2(z = S) - \omega^2}}, \tag{5}$$

subject to $S(x_0) = z_0$. Here, $N = N(z)$ is the Brunt-Väisälä or buoyancy frequency and $\omega = 2\pi/T$ is the angular frequency of the wave, with T being its period. When a ray path encounters a boundary, it is terminated at the point of intersection.

The frequency of the wave will correspond to the frequency of the forcing, that is, that of the MJO. Ray paths are superimposed on Figure 11 for two different frequencies, corresponding to $T = 30$ day (high-frequency end of MJO forcing; dashed blue lines) and $T = 60$ day (low-frequency end of MJO forcing; solid blue lines). The sample ray paths are initiated at 50 m depth (the nominal top of the thermocline, where wave propagation will become well established) and at selected longitudes. The $T = 60$ day period ray paths track the observed phase lines (e.g., boundary between negative and positive vertical displacement anomalies) well, down into the deep ocean, again emphasizing the importance of the low-frequency end of the MJO forcing for generating deep ocean wave responses. For example, the $T = 60$ day period ray paths initiated at 140°E and 140°W during MJO phase 5 (Figure 11e) track the western and eastern boundaries of the positive vertical displacement anomaly in the central Pacific very well. Hence, the deep MJO ocean dynamical anomalies are well explained by this vertically propagating Kelvin wave framework.

Ray paths are also initiated at the western boundary in each ocean basin (the thicker solid blue lines for the $T = 60$ day forcing). Given that the (near) surface at the western boundary is the furthest west that a Kelvin wave can be initiated, and the Kelvin wave then propagates eastward and downward along the ray path, these ray paths define the border of "shadow zones" in the deep western basins, where no Kelvin wave can penetrate (Amol et al., 2022). Indeed, there are no coherent anomalies within these shadow zones in Figure 11, just small-scale noise.

The Pacific basin is wide enough such that the shadow zone at 2,000 m depth (boundary at 180°E) covers only approximately 1/3 of the basin, and Kelvin waves can and do reach 2,000 m in the eastern 2/3 of the basin. Evidence for this is provided by the frequency spectra of potential density at 1,062 m at two selected locations in the Pacific (Figure S2 in Supporting Information S1). They show the expected red noise background, with higher

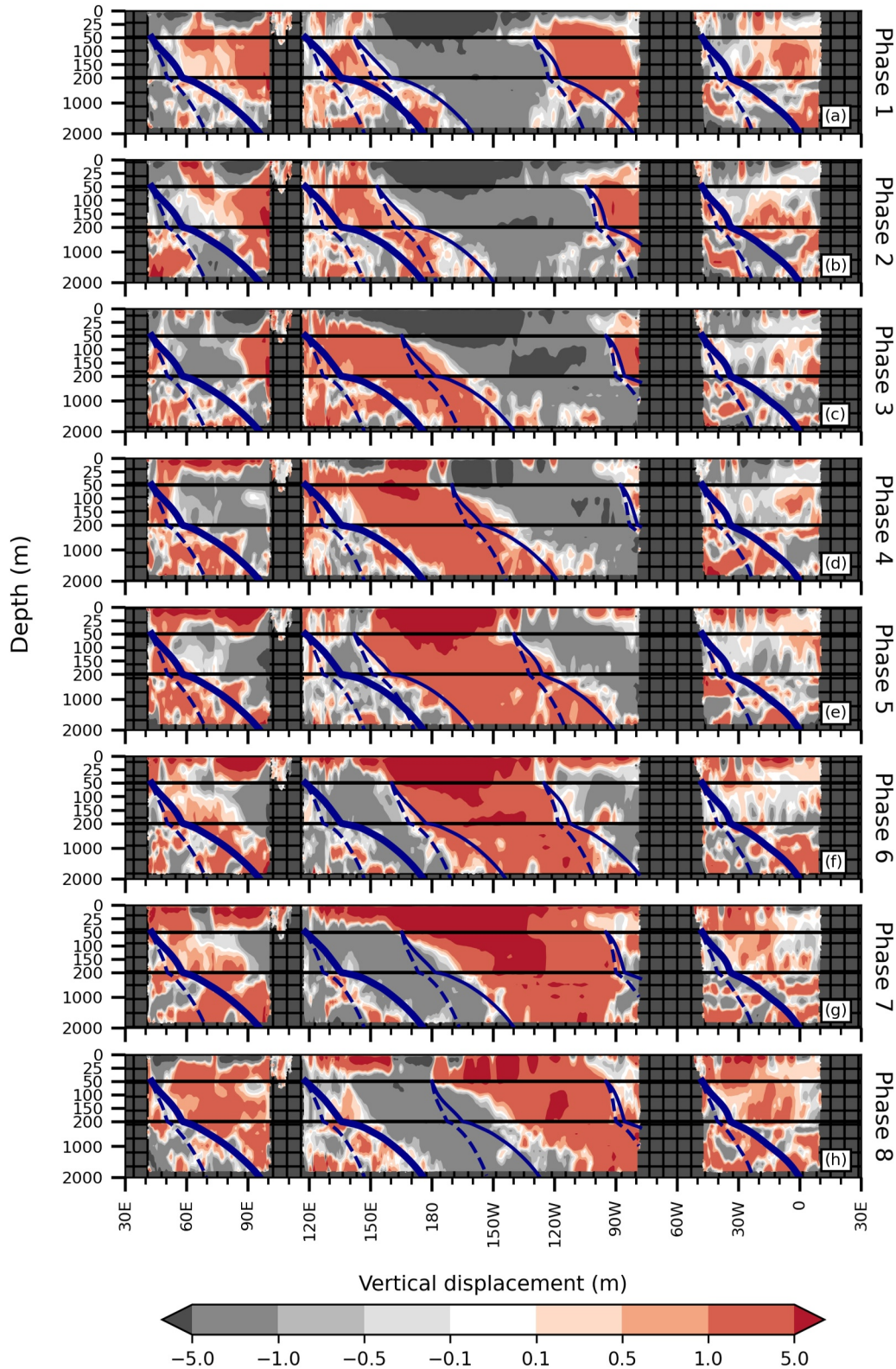

Figure 11. Longitude-depth sections of inferred vertical displacement (color shading) at the equator (averaged 1.5°S–1.5°N) during the MJO cycle. The blue lines indicate selected Kelvin wave ray paths for different wave periods (dashed $T = 30$ days; solid $T = 60$ days; thick solid $T = 60$ days starting at the surface on the western boundary of each ocean basin).

magnitude at lower frequencies. Additionally, the frequency spectrum at 120.2°W in the eastern Pacific shows a peak above this background at frequencies corresponding to periods near 60 days, distinct from surrounding frequency bands. This longitude is outside the shadow zone and therefore susceptible to wave energy propagating in at the low-frequency end of the MJO forcing range. In contrast, the frequency spectrum at 149.8°E in the western Pacific does not show such a peak. This longitude lies inside the shadow zone we have identified and therefore it is consistent with our argument that it does not contain wave energy forced by the MJO.

The Indian Ocean basin is much narrower, and the shadow zone almost reaches the eastern boundary at 2,000 m. Hence, the coherent MJO (Kelvin wave) signal only reaches 2,000 m depth at the very eastern end of the Indian Ocean basin. The Atlantic basin is similarly narrow and would be affected by the same extensive shadow zone. However, the MJO wind forcing is much weaker anyway in this basin and there is no coherent deep ocean response anywhere in the equatorial Atlantic basin.

6. Discussion and Conclusions

Previous work on the equatorial deep ocean structure of the MJO has been limited to an analysis of temperature and salinity data from the first three years of the Argo float program from 2003 to 2006 down to a maximum depth between 1,000 and 1,400 m (Matthews et al., 2007, 2010). They found a deep ocean structure of the MJO consistent with an equatorial Kelvin wave structure. Here, we have extended those analyses using 18 years (2003–2018) of data down to 2,000 m depth, using an ocean reanalysis assimilating Argo data. The MJO temperature and salinity structures of Matthews et al. (2010) were confirmed by this extended study, with the deep ocean signals being more coherent due to the longer data set used.

Moreover, as the ocean reanalysis is a dynamically consistent data set, its ocean currents are in balance with the observed temperature and salinity fields. Hence, the deep ocean current anomalies associated with the MJO were able to be analyzed across the three equatorial ocean basins for the first time. Coherent MJO equatorial zonal current anomalies of over 1 cm s^{-1} were found to extend into the deep ocean down to 2,000 m depth. Furthermore, as the ocean analysis fields are dynamically consistent, the deep ocean dynamical response to MJO surface forcing can be diagnosed and interpreted using theoretical frameworks. Two frameworks were investigated: vertical modes and vertically propagating waves.

In the thermocline depth range, the MJO anomalies were interpreted using a vertical mode framework. The vertical and horizontal structures of the thermocline anomalies were best explained by a first internal mode Kelvin wave structure. However, the observed eastward propagation speed of the anomalies (3.4 m s^{-1}) was slightly faster than the theoretical eastward propagation speed of the first internal mode (2.7 m s^{-1}). This discrepancy was modeled as a combination of the forced response to the MJO wind stress forcing, which propagates eastward at approximately 5 m s^{-1} over the western Pacific and up to 15 m s^{-1} over the eastern Pacific, and the free wave response at 2.7 m s^{-1}. Energy was also found in higher modes, particularly the second and third internal modes. Hence, a pure single vertical mode response was not found. This was likely due to nonlinear interactions resulting in a transfer of energy from the first mode to higher modes. Similar results have been found in previous studies of intraseasonal equatorial Kelvin waves in the thermocline. Previous research shows that structures are dominated by the first internal mode in the Pacific (Hendon et al., 1998) and the second internal mode in the Indian Ocean (Pujiana & McPhaden, 2020), with other vertical modes also being non-negligible.

However, in the deep ocean below the thermocline (the main focus of this paper), the vertical mode framework does not account for the observed MJO structure, in particular the eastward and downward tilt of the phase lines. Here, a vertically propagating wave framework was needed. In particular, theoretical Kelvin ray paths with a period of 60 days (at the low-frequency end of the broad spectrum 30–60-day period surface forcing from the MJO) accounted for the observed eastward and downward phase tilts. This preferential response to the low-frequency component of the MJO forcing has also been found for anomalies in the thermocline (Hendon et al., 1998; Nagura & McPhaden, 2012). Hence, it appears here that this preferential response also extends to the downward-propagating Kelvin waves in the deeper ocean.

The combination of downward and eastward tilting phase lines emanating from the MJO forcing at the surface, and the existence of the topographic barriers of Africa, the Maritime Continent, and South America, lead to the existence of shadow zones in the deep Indian, Pacific, and Atlantic Oceans at their western boundaries, where no downward-propagating Kelvin wave can reach. The observed deep ocean MJO anomalies are consistent with the

existence of these shadow zones, as no coherent anomalies are observed within them, whereas immediately to the east of the theoretical shadow zones, coherent MJO anomalies are observed and a peak is produced in the frequency spectra around 60 days. The extent of these shadow zones is significant. At 2,000 m depth, they extend approximately 50° longitude into an ocean basin. As both the Indian and Atlantic basins are only 60° longitude wide at the equator, this means that in these basins, MJO anomalies are only able to penetrate down to 2,000 m depth in the far east of each basin. Independently, Amol et al. (2022) found much higher intraseasonal current variability in the deep ocean from moorings in the eastern Indian Ocean (93°E) than in moorings further west, supporting the existence of these shadow zones. The Pacific basin is significantly wider (spanning 160° longitude at the equator) than the Indian and Atlantic basins. As a result, MJO anomalies are able to penetrate the deep Pacific Ocean over most of the basin. At even greater depths, near 4,000 m, shadow zones have been found in the *eastern* side of the basins (Amol et al., 2022). The variability at these depths was mainly due to equatorial Rossby waves, which propagate westward. These Rossby waves were triggered by the reflection of downward-propagating Kelvin waves when they reached the eastern boundary.

What are the implications of these MJO deep ocean anomalies? The implied vertical displacements from these deep ocean MJO anomalies are moderate, with amplitudes of a few meters. Although the implied vertical displacements in the deep ocean are moderate, these are values derived from a composite mean study of multiple MJO events. Due especially to the broad-band nature of MJO forcing (e.g., 30–60-day periods), there will be partial destructive interference between events with different periods, and the anomalies observed in individual MJO events may be larger, by up to a factor of 2–3 (Matthews et al., 2007), compared with O (10) m for internal tides in this region (Wang et al., 2023).

However, the 30–60-day period for these deep MJO waves is much longer than that for typical internal gravity waves. Because of their low frequency and long horizontal wavelengths (5,000–10,000 km), the dissipation of these MJO waves is likely to occur remotely from their source, as evidenced by their propagation across the basins and into the deep ocean. Ultimately, these waves must dissipate; hence, the MJO may have a role to play in deep-ocean mixing, an important yet poorly understood component of the global climate system. Ocean modeling indicates that vertically propagating equatorially trapped waves can reflect off the ocean bottom into short inertia-gravity waves and produce an environment of high vertical shear and low Richardson number (Delorme & Thomas, 2019). This leads to significant mixing and is an important component in the abyssal overturning circulation. These processes occur over a smooth ocean bottom, that is, they do not require significant bottom topography, as is the case over much of the eastern equatorial Pacific. The vertically propagating Kelvin waves forced by the MJO over the Pacific may inject energy into the deep ocean and thus contribute to these mixing processes. Due to the large shadow zones in the Indian and Atlantic basins, the role of the MJO in deep-ocean mixing in these basins may be smaller, though subsequent reflection at the eastern boundaries and downward propagation as equatorial Rossby waves may still be relevant here.

Climate models often fail to realistically simulate the MJO, with many models exhibiting MJO variability that is too weak and that does not propagate eastward realistically (Hung et al., 2013). Furthermore, models often fail to accurately simulate the distribution and variability of intraseasonal Kelvin waves, with these modeled waves propagating more slowly than observations (Cui et al., 2024). As a result, the deep ocean variability generated by MJO-forced Kelvin waves will be too weak, with a knock-on impact on the simulation of deep-ocean mixing. Hence, as energy propagation into the deep ocean is a mechanism by which the surface signature of the MJO will decay, correct simulation of these deep ocean processes will be relevant to MJO simulation in general and forecasting in particular. There are also implications for oceanographic observational programs in the equatorial regions, especially those where observations are time-limited. Care should be taken to ascertain the strength and phase of the MJO during the observational period and take into account its possible effect on deep water processes during the campaign.

Several lines of future work are suggested here. When the horizontally propagating MJO-forced equatorial Kelvin waves in the thermocline impact on the eastern ocean boundary, they can both reflect into westward propagating equatorial Rossby waves and transform into poleward propagating coastally trapped Kelvin waves (Webber, Stevens, et al., 2012). Further work is needed to determine the fate of these MJO-forced vertically propagating waves in the deep ocean when they impact on the eastern boundary or on bottom topography. Is energy absorbed (Delorme & Thomas, 2019) or reflected (Amol et al., 2022)? What are the implications for ocean mixing? Remote impacts (as in the deep ocean) from the MJO are notoriously difficult to diagnose due to the broad-band nature of

the MJO forcing. As noted in the footnote above, different individual MJO events with different time scales can partially cancel when simple composites are calculated, as in this study. Recently, Green's function approaches have been used to diagnose remote responses to forcing in the ocean (Kostov et al., 2017) and atmosphere (Deb et al., 2020; Sen et al., 2024). Such an approach could be usefully applied to the deep ocean response to the MJO to remediate this broad-band forcing problem.

Data Availability Statement

This study has been conducted using E.U. Copernicus Marine Service Information; the GLORYS12V1 ocean reanalysis data were downloaded from GLORYS12V1, E.U. Copernicus Marine Service Information (CMEMS), Marine Data Store (MDS), 10.48670/moi-00021 (accessed between 01-02-2024 and 09-02-2024). The vertical modes were calculated using the Dynmodes package, downloaded from https://www.eoas.ubc.ca/~sallen/AIMS-workshop/_modules/dynmodes.html, accessed on 20 February 2024, an implementation in Python of the original Dynmodes package by John Klinck, 1999, which can be found at https://github.com/sea-mat/dynmodes. The TAO/TRITON and RAMA mooring data were downloaded from the NOAA/PMEL GTMBA Project Office at https://www.pmel.noaa.gov/gtmba/pmel-theme/pacific-ocean-tao.

Acknowledgments
We thank the three reviewers for their constructive comments that helped to improve the manuscript. C.R. was funded, and A.J.M., R.H., and K.J.H. were partially funded, by the UK Natural Environment Research Council (NERC) TerraMaris project (Grant NE/R016704/1). The research presented in this paper was carried out on the High Performance Computing Cluster supported by the Research Computing Service at the University of East Anglia.

References

Amol, P., Jain, V., & Aparna, S. G. (2022). Blue-shifted deep ocean currents in the equatorial Indian Ocean. *Climate Dynamics*, *59*(1), 219–229. https://doi.org/10.1007/s00382-021-06125-9

Bernie, D. J., Guilyardi, E., Madec, G., Slingo, J. M., Woolnough, S. J., & Cole, J. (2008). Impact of resolving the diurnal cycle in an ocean-atmosphere GCM. Part 2: A diurnally coupled CGCM. *Climate Dynamics*, *31*(7–8), 909–925. https://doi.org/10.1007/s00382-008-0429-z

Chelton, D. B., DeSzoeke, R. A., Schlax, M. G., El Naggar, K., & Siwertz, N. (1998). Geographical variability of the first baroclinic Rossby radius of deformation. *Journal of Physical Oceanography*, *28*(3), 433–460. https://doi.org/10.1175/1520-0485(1998)028<0433:gvotfb>2.0.co;2

Chi, N.-H., Lien, R.-C., D'Asaro, E. A., & Ma, B. B. (2014). The surface mixed layer heat budget from mooring observations in the central Indian Ocean during Madden–Julian Oscillation events. *Journal of Geophysical Research: Oceans*, *119*(7), 4638–4652. https://doi.org/10.1002/2014jc010192

Cravatte, S., Picaut, J., & Eldin, G. (2003). Second and first baroclinic Kelvin modes in the equatorial Pacific at intraseasonal time scales. *Journal of Geophysical Research*, *108*(C8), 3266. https://doi.org/10.1029/2002JC001511

Cui, J., DeMott, C., Riley Dellaripa, E., & Maloney, E. (2024). Process-based evaluation of intraseasonal oceanic Kelvin waves in the Pacific Ocean in CMIP6 models. *Journal of Climate*, *37*(23), 6435–6452. https://doi.org/10.1175/jcli-d-23-0668.1

Da Silva, N. A., & Matthews, A. J. (2021). Impact of the Madden–Julian Oscillation on extreme precipitation over the western Maritime Continent and Southeast Asia. *Quarterly Journal of the Royal Meteorological Society*, *147*(739), 3434–3453. https://doi.org/10.1002/qj.4136

Deb, P., Matthews, A. J., Joshi, M. M., & Senior, N. (2020). The extratropical linear step response to tropical precipitation anomalies and its use in constraining projected circulation changes under climate warming. *Journal of Climate*, *33*(16), 7217–7231. https://doi.org/10.1175/JCLI-D-20-0060.1

Delorme, B., & Thomas, L. (2019). Abyssal mixing through critical reflection of equatorially trapped waves off smooth topography. *Journal of Physical Oceanography*, *49*(2), 519–542. https://doi.org/10.1175/jpo-D-18-0197.1

DeMott, C. A., Klingaman, N. P., & Woolnough, S. J. (2015). Atmosphere-ocean coupled processes in the Madden–Julian Oscillation. *Reviews of Geophysics*, *53*(4), 1099–1154. https://doi.org/10.1002/2014RG000478

Foltz, G. R., & McPhaden, M. J. (2004). The 30–70 day oscillations in the tropical Atlantic. *Geophysical Research Letters*, *31*(15). https://doi.org/10.1029/2004gl020023

Hendon, H. H., Liebmann, B., & Glick, J. D. (1998). Oceanic Kelvin waves and the Madden–Julian oscillation. *Journal of the Atmospheric Sciences*, *55*(1), 88–101. https://doi.org/10.1175/1520-0469(1998)055<0088:okwatm>2.0.co;2

Hersbach, H., Bell, B., Berrisford, P., Hirahara, S., Horányi, A., Muñoz-Sabater, J., et al. (2020). The ERA5 global reanalysis. *Quarterly Journal of the Royal Meteorological Society*, *146*(730), 1999–2049. https://doi.org/10.1002/qj.3803

Holton, J. R., & Hakim, G. J. (2012). *An introduction to dynamic meteorology*. Academic Press.

Huang, K., Han, W., Wang, D., Wang, W., Xie, Q., Chen, J., & Chen, G. (2018). Features of the equatorial intermediate current associated with basin resonance in the Indian Ocean. *Journal of Physical Oceanography*, *48*(6), 1333–1347. https://doi.org/10.1175/JPO-D-17-0238.1

Hung, M. P., Lin, J. L., Wang, W., Kim, D., Shinoda, T., & Weaver, S. J. (2013). MJO and convectively coupled equatorial waves simulated by CMIP5 climate models. *Journal of Climate*, *26*(17), 6185–6214. https://doi.org/10.1175/JCLI-D-12-00541.1

Iskandar, I., & McPhaden, M. J. (2011). Dynamics of wind-forced intraseasonal zonal current variations in the equatorial Indian Ocean. *Journal of Geophysical Research*, *116*(C6), C06019. https://doi.org/10.1029/2010jc006864

Jiang, X., Adames, Á. F., Kim, D., Maloney, E. D., Lin, H., Kim, H., et al. (2020). Fifty years of research on the Madden–Julian oscillation: Recent progress, challenges, and perspectives. *Journal of Geophysical Research: Atmospheres*, *125*(17), e2019JD030911. https://doi.org/10.1029/2019JD030911

Johnson, E. S., & McPhaden, M. J. (1993). Effects of a three-dimensional mean flow on intraseasonal Kelvin waves in the equatorial Pacific Ocean. *Journal of Geophysical Research*, *98*(C6), 10185–10194. https://doi.org/10.1029/93jc00759

Karlowska, E., Matthews, A. J., Webber, B. G. M., Graham, T., & Xavier, P. (2024a). The effect of diurnal warming of sea surface temperatures on the propagation speed of the Madden–Julian Oscillation. *Quarterly Journal of the Royal Meteorological Society*, *150*(758), 334–354. https://doi.org/10.1002/qj.4599

Karlowska, E., Matthews, A. J., Webber, B. G. M., Graham, T., & Xavier, T. (2024b). Two-way feedback between the Madden–Julian Oscillation and diurnal warm layers in a coupled ocean-atmosphere model. *Quarterly Journal of the Royal Meteorological Society*, *99*(764), 4113–4132. https://doi.org/10.1002/qj.4807

Karnauskas, K. B., Murtugudde, R., & Busalacchi, A. J. (2007). The effect of the Galápagos islands on the equatorial Pacific cold tongue. *Journal of Physical Oceanography*, *37*(5), 1266–1281. https://doi.org/10.1175/jpo3048.1

Kent, C., Scaife, A. A., & Dunstone, N. (2022). What potential for improving sub-seasonal predictions of the winter NAO? *Atmospheric Science Letters*, *24*(4), e1146. https://doi.org/10.1002/asl.1146

Kessler, W. S., & McPhaden, M. J. (1995). Oceanic equatorial waves and the 1991–93 El Niño. *Journal of Climate*, *8*(7), 1757–1774. https://doi.org/10.1175/1520-0442(1995)008⟨1757:OEWATE⟩2.0.CO;2

Kessler, W. S., McPhaden, M. J., & Weickmann, K. M. (1995). Forcing of intraseasonal Kelvin waves in the equatorial Pacific. *Journal of Geophysical Research*, *100*(C6), 10613–10631. https://doi.org/10.1029/95jc00382

Kostov, Y., Marshall, J., Hausmann, U., Armour, K. C., Ferreira, D., & Holland, M. M. (2017). Fast and slow responses of Southern Ocean sea surface temperature to SAM in coupled climate models. *Climate Dynamics*, *48*(5–6), 1595–1609. https://doi.org/10.1007/s00382-016-3162-z

Kutsuwada, K., & McPhaden, M. J. (2002). Intraseasonal variations in the upper equatorial Pacific Ocean prior to and during the 1997–98 El Niño. *Journal of Physical Oceanography*, *32*(4), 1133–1149. https://doi.org/10.1175/1520-0485(2002)032<1133:ivitue>2.0.co;2

Lellouche, J.-M., Greiner, E., Bourdallé-Badie, R., Garric, G., Melet, A., Drévillon, M., et al. (2021). The copernicus global 1/12° oceanic and sea ice GLORYS12 reanalysis. *Frontiers in Earth Science*, *9*, 698876. https://doi.org/10.3389/feart.2021.698876

Madden, R. A., & Julian, P. R. (1972). Description of global-scale circulation cells in the tropics with a 40–50 day period. *Journal of the Atmospheric Sciences*, *29*(6), 1109–1123. https://doi.org/10.1175/1520-0469(1972)029<1109:dogscc>2.0.co;2

Matthews, A. J. (2000). Propagation mechanisms for the Madden–Julian Oscillation. *Quarterly Journal of the Royal Meteorological Society*, *126*(569), 2637–2652. https://doi.org/10.1256/smsqj.56901

Matthews, A. J., Singhruck, P., & Heywood, K. J. (2007). Deep ocean impact of a Madden–Julian oscillation observed by Argo floats. *Science*, *318*(5857), 1765–1769. https://doi.org/10.1126/science.1147312

Matthews, A. J., Singhruck, P., & Heywood, K. J. (2010). Ocean temperature and salinity components of the Madden–Julian oscillation observed by Argo floats. *Climate Dynamics*, *35*(7–8), 1149–1168. https://doi.org/10.1007/s00382-009-0631-7

Matthews, A. J., Slingo, J. M., Hoskins, B. J., & Inness, P. M. (1999). Fast and slow Kelvin waves in the Madden–Julian oscillation of a GCM. *Quarterly Journal of the Royal Meteorological Society*, *125*(557), 1473–1498. https://doi.org/10.1256/smsqj.55701

McCreary, J. P., Jr. (1984). Equatorial beams. *Journal of Marine Research*, *42*(2), 395–430. https://doi.org/10.1357/002224084788502792

McPhaden, M. J. (1999). Genesis and evolution of the 1997-98 El Niño. *Science*, *283*(5404), 950–954. https://doi.org/10.1126/science.283.5404.950

McPhaden, M. J. (2002). Mixed layer temperature balance on intraseasonal timescales in the equatorial Pacific Ocean. *Journal of Climate*, *15*(18), 2632–2647. https://doi.org/10.1175/1520-0442(2002)015<2632:mltboi>2.0.co;2

McPhaden, M. J., Proehl, J., & Rothstein, L. (1987). On the structure of low-frequency equatorial waves. *Journal of Physical Oceanography*, *17*(9), 1555–1559. https://doi.org/10.1175/1520-0485(1987)017<1555:otsolf>2.0.co;2

McPhaden, M. J., & Ripa, P. (1990). Wave-mean flow interactions in the equatorial ocean. *Annual Review of Fluid Mechanics*, *22*(1), 167–206. https://doi.org/10.1146/annurev.fl.22.010190.001123

McPhaden, M. J., & Yu, X. (1999). Equatorial waves and the 1997–98 El Niño. *Geophysical Research Letters*, *26*(19), 2961–2964. https://doi.org/10.1029/1999gl004901

Nagura, M., & McPhaden, M. J. (2012). The dynamics of wind-driven intraseasonal variability in the equatorial Indian Ocean. *Journal of Geophysical Research*, *117*(C2), C02001. https://doi.org/10.1029/2011JC007405

Philander, S. (1978). Forced oceanic waves. *Reviews of Geophysics*, *16*(1), 15–46. https://doi.org/10.1029/rg016i001p00015

Pujiana, K., & McPhaden, M. J. (2020). Intraseasonal Kelvin waves in the equatorial Indian Ocean and their propagation into the Indonesian seas. *Journal of Geophysical Research: Oceans*, *125*(5), e2019JC015839. https://doi.org/10.1029/2019JC015839

Roundy, P. E., & Kiladis, G. N. (2006). Observed relationships between oceanic Kelvin waves and atmospheric forcing. *Journal of Climate*, *19*(20), 5253–5272. https://doi.org/10.1175/JCLI3893.1

Roxy, M., Dasgupta, P., McPhaden, M. J., Suematsu, T., Zhang, C., & Kim, D. (2019). Twofold expansion of the Indo-Pacific warm pool warps the MJO life cycle. *Nature*, *575*(7784), 647–651. https://doi.org/10.1038/s41586-019-1764-4

Rydbeck, A. V., & Jensen, T. G. (2017). Oceanic impetus for convective onset of the Madden–Julian oscillation in the western Indian Ocean. *Journal of Climate*, *30*(11), 4299–4316. https://doi.org/10.1175/jcli-d-16-0595.1

Rydbeck, A. V., Jensen, T. G., & Flatau, M. (2019). Characterization of intraseasonal Kelvin waves in the equatorial Pacific Ocean. *Journal of Geophysical Research: Oceans*, *124*(3), 2028–2053. https://doi.org/10.1029/2018JC014838

Rydbeck, A. V., Jensen, T. G., & Nyadjro, E. S. (2017). Intraseasonal sea surface warming in the western Indian Ocean by oceanic equatorial Rossby waves. *Geophysical Research Letters*, *44*(9), 4224–4232. https://doi.org/10.1002/2017gl073331

Sen, A., Deb, P., Matthews, A. J., & Joshi, M. M. (2024). Teleconnection and the Antarctic response to the Indian Ocean Dipole in CMIP5 and CMIP6 models. *Quarterly Journal of the Royal Meteorological Society*, *99*(765), 5020–5036. https://doi.org/10.1002/qj.4854

Wang, Y., Xu, Z., Li, Q., Chen, Z., You, J., Yin, B., & Robertson, R. (2023). Observed internal tides in the deep northwestern Pacific by Argo floats. *Deep-Sea Research II*, *207*, 105248. https://doi.org/10.1016/j.dsr2.2022.105248

Webber, B. G. M., Matthews, A. J., & Heywood, K. J. (2010). A dynamical ocean feedback mechanism for the Madden–Julian oscillation. *Quarterly Journal of the Royal Meteorological Society*, *136*(648), 740–754. https://doi.org/10.1002/qj.604

Webber, B. G. M., Matthews, A. J., Heywood, K. J., & Stevens, D. P. (2012). Ocean Rossby waves as a triggering mechanism for primary Madden–Julian events. *Quarterly Journal of the Royal Meteorological Society*, *138*(663), 514–527. https://doi.org/10.1002/qj.936

Webber, B. G. M., Stevens, D. P., Matthews, A. J., & Heywood, K. J. (2012). Dynamical ocean forcing of the Madden–Julian oscillation at lead times of up to five months. *Journal of Climate*, *25*(8), 2824–2842. https://doi.org/10.1175/jcli-d-11-00268.1

Wheeler, M. C., & Hendon, H. H. (2004). An all-season real-time multivariate MJO index: Development of an index for monitoring and prediction. *Monthly Weather Review*, *132*(8), 1917–1932. https://doi.org/10.1175/1520-0493(2004)132<1917:aarmmi>2.0.co;2

Wong, A. P. S., Other, A. N., Other, A. N. O., Pouliquen, S., Hosoda, S., Roemmich, D., et al. (2020). Argo data 1999-2019: Two million temperature-salinity profiles and subsurface velocity observations from a global array of profiling floats. *Frontiers in Marine Science*, *7*, 700. https://doi.org/10.3389/fmars.2020.00700

Woolnough, S. J., Vitart, F., & Balmaseda, M. A. (2007). The role of the ocean in the Madden–Julian Oscillation: Implications for MJO prediction. *Quarterly Journal of the Royal Meteorological Society*, *133*(622), 117–128. https://doi.org/10.1002/qj.4

Xie, S.-P. (2024). Chapter 7 - Equatorial oceanography. In S.-P. Xie (Ed.), *Coupled atmosphere-ocean dynamics* (pp. 165–187). Elsevier. https://doi.org/10.1016/B978-0-323-95490-7.00007-2

Zhang, C. (2005). Madden–Julian oscillation. *Reviews of Geophysics*, *43*(2), RG2003. https://doi.org/10.1029/2004RG000158

Zhang, C., Adames, Á. F., Khouider, B., Wang, B., & Yang, D. (2020). Four theories of the Madden–Julian oscillation. *Reviews of Geophysics*, *58*(3), e2019RG000685. https://doi.org/10.1029/2019rg000685